JOURNAL OF PROPULSION AND POWER
Vol. 20, No. 2, March–April 2004

Modeling and Analysis of a Megawatt-Class Magnetoplasmadynamic Thruster

Pavlos G. Mikellides*
Arizona State University, Tempe, Arizona 85287

The magnetohydrodynamic code MACH2 is utilized to investigate the operation and performance of a megawatt-class, quasi-steady, self-field magnetoplasmadynamic thruster. The numerical results are validated by comparisons to experimental data and offer significant insights into this regime of operation. Specifically, operation at 0.5–6 MW and 1.37 g/s shows incomplete hydrogen-propellant ionization that is dominated by electron–neutral collisions, which in turn increase the plasma voltage, but do not substantially increase thrust. Acceleration is of a hybrid nature, transitioning from primarily electrothermal to predominantly electromagnetic with increasing current level. Detailed interrogation of energy deposition shows significant deposition to internal modes, as opposed to external-circuit-element losses and electrode losses via fall voltage and thermal conduction, even at the higher power levels. These frozen-flow and radial-momentum losses can be reduced while the system still operates with minimum power penalty by proper expansion of the flow.

Nomenclature

A	=	area
a_0	=	ion acoustic speed
B	=	magnetic field
e	=	specific energy
J	=	current
$\mathring{m}$	=	mass-flow rate
P	=	power
Q	=	ionization energy
q	=	elementary charge
r_a, r_c	=	anode, cathode radius
T	=	thrust
U	=	velocity
γ	=	ratio of specific heats
δ	=	current distribution parameter
ζ	=	average charge
$\tilde{\eta}$	=	magnetic diffusivity
κ	=	thermal conductivity
μ_0	=	permeability of free space
ρ	=	density
σ_e	=	electron-atom collision cross-section

Introduction

ELECTROMAGNETIC acceleration with and without externally applied magnetic fields has traditionally been a very attractive concept for a variety of space missions ranging from orbital maneuvering to interplanetary travel. The basic acceleration mechanism for thrusters without external magnetic fields is twofold-electromagnetic and electrothermal. The relative significance of each of these two force components depends on the power level and mass-flow-rate operation. The current generated by the applied voltage differential between the electrodes induces an azimuthal magnetic field, which in turn interacts with the current to produce an axially directed electromagnetic force, known as the Lorentz force [see Fig. 1(top)]. This electromagnetic component has traditionally been approximated by the Maecker formula,[1]

$$T_{\mathrm{EM}} = \left(\mu_0 J^2 \big/ 4\pi\right)[\ell_n(r_a/r_c) + \delta], \qquad \tfrac{1}{2} \le \delta \le \tfrac{3}{4} \tag{1}$$

where the parameter δ is chosen based on the current distribution over the cathode surface.[2] In addition, the applied current heats the plasma via Ohmic heating, which generates an electrothermal-force component as the gas expands to vacuum conditions. The Maecker formula was improved by Tikhonov,[3] who included thermal pressure contributions and was able to capture total-thrust trends for a wider range of $J^2/\mathring{m}$:

$$T = \frac{(\gamma+1)\mu_0 J^2}{8\pi} + \frac{8\pi a_0^2 \dot{m}^2}{\gamma^2 \mu_0 J^2} \tag{2}$$

where the ion acoustic speed a_0 has to be arbitrarily chosen at the upstream location of the current conduction zone.

The thruster is relatively simple to operate within a robust configuration that diminishes component failure and maintenance issues. When operated in the megawatt power range it can provide intermediate values for specific impulse (2000–7000 s) and thrust (50–100 N) that compete with both chemically aerobraked and electrothermally dominated systems as well as ion and Hall thrusters.

However, the self-field magnetoplasmadynamic (MPD) thruster has to consistently operate at efficiencies exceeding 50% and demonstrate the necessary lifetimes to provide the payload and trip-time advantages associated with the aforementioned performance capabilities.[4,5] Even though it has been rigorously researched for the past forty years, such efficient implementation still eludes us. To date, our accomplishments and understanding of self-field megawatt-MPD operation are limited to the following, largely empirical findings:

Performance improves with increasing power levels; the highest reported cases demonstrated 40% efficiency at 1.5 MW (Ref. 6) and 55% at 15 MW (Ref. 7). The inefficiencies have been attributed to frozen-flow and electrode losses via fall voltage and thermal conduction. Furthermore, the self-field MPD thruster demonstrates a limitation as power is increased, the so-called "onset," which is manifested by voltage fluctuations and elevated electrode erosion.[7] This phenomenon, which scales with $J^2/\mathring{m}$ among other parameters,[8] degrades performance at higher power levels and leads to thruster failure. The latter is indeed the ultimate performance ceiling. Missions of interest require operation for thousands of hours, whereas the longest demonstrated test did not exceed 500 h (Ref. 9).

Numerical efforts have progressed more slowly than empirical research, mainly due to lack of the computational resources necessary to properly model the highly nonlinear and interactive physics involved in the accelerator. Only recently have these capabilities become available and allowed application of two-dimensional planar and cylindrical magnetohydrodynamic (MHD) codes to the MPD

Received 18 June 2002; revision received 20 March 2003; accepted for publication 22 October 2003.

*Assistant Professor, Department of Mechanical and Aerospace Engineering, P.O. Box 876106; Pavlos.Mikellides@asu.edu. Member AIAA.

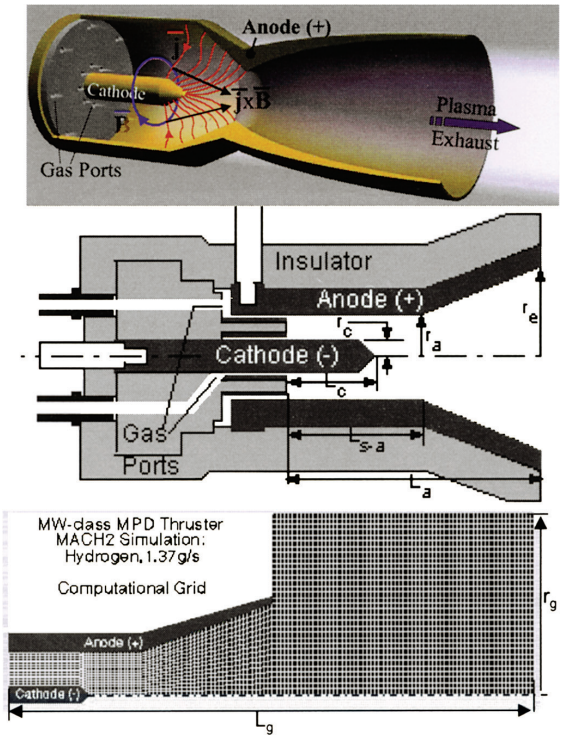

Fig. 1 Top: Schematic of a MPD thruster configuration depicting electromagnetic acceleration mechanism. Middle: Schematic of the multimegawatt MY-II MPD thruster simulated by MACH2. Bottom: MACH2 computational region and grid. Dimensions in mm: $r_c = 4.75$, $r_a = 25$, $r_e = 52$, $L_c = 45$, $L_{s-a} = 75$, $L_a = 104$, $L_g = 300$, $r_g = 104$.

problem. A comprehensive discussion of the numerical efforts is summarized in Ref. 5. Even though they have provided numerous and valuable insights, our confidence in their validity and completeness is still burdened by skepticism. Such rigorous and confirmed theory is absolutely necessary not only to enhance our comprehension of overall or isolated MPD processes, but ultimately to be utilized to design real and better thrusters.

The present effort aims to apply a cultured MHD numerical code to the self-field MPD problem with the ultimate goal in mind of providing specific directions for performance improvement. The MHD code MACH2 has been utilized previously to examine applied-field MPD acceleration with great success.[10] In that effort, preliminary self-field simulations provided confidence when compared to experimentally deduced current distributions.[11] Besides being a full two-dimensional axisymmetric code that can simulate real thruster geometries and real plasmas, it includes unique transport models that have been essential in deciphering applied-field operation at sub-100-kW levels. Specifically, this previous research has completely altered the traditional perception of magnetic nozzle operation, but most important has outlined thruster designs that will consistently operate at elevated efficiencies.[12] This paper proceeds to validate MACH2 by comparisons with experimental data including two-dimensional current distribution, identify significant physics and the magnitude of the dominant energy-loss mechanisms, and propose directions for improved thruster efficiency in the megawatt power range.

Numerical Model

In the mid-1980s a magnetohydrodynamics (MHD) code was developed to study collisional plasmas for problems of complex geometries.[13] Over the years, this multiblock arbitrary-coordinate hydromagnetic (MACH) simulation tool has been utilized to model a diverse range of plasma problems and has been substantially upgraded through contributions from a variety of research efforts.

MACH2 is a time-dependent, two-dimensional, axisymmetric, multimaterial code that can be applied to problems of complex geometries due to its multiblock structure.[14] The computational mesh can move in an arbitrary Lagrangian–Eulerian fashion that allows applicability to both diffusion- and dispersion-dominated problems as well as code validation. The mesh can be refined via a variety of adaptive schemes to capture regions of varying characteristic scale. The set of single-fluid MHD equations is time-advanced with finite volume spacial differencing, and the boundary conditions are applied via the ghost-cell technique so that no special conditional statement is necessary at the boundaries. One of the advantages of the MACH2 code is that diffusion processes are numerically differenced using implicit schemes that are not limited by restrictive Courant numbers. Specifically, the processes of thermal and magnetic diffusion are computed via an iterative Jacobi method that uses a multigrid algorithm to increase its convergence rate.[13]

The mass continuity and momentum equations assume a compressible, viscous fluid. The stress deviator can be chosen to evolve under elastic stress for strength-of-materials calculations[15] or modeled as a Newtonian fluid to upgrade the code to a Navier–Stokes solver.[11] The electrons, ions, and radiation field are in thermal nonequilibrium, so MACH2 solves up to three energy equations. These include thermal conduction with anisotropic transport[16] and three different models for radiation cooling.[17,18] Evolution of the magnetic field is prescribed by the magnetic induction equation

$$\frac{\partial \boldsymbol{B}}{\partial t} = \nabla \times (\boldsymbol{v} \times \boldsymbol{B}) - \nabla \times \left(\frac{\eta}{\mu_0} \nabla \times \boldsymbol{B} \right) - \nabla \times \left[\frac{(\nabla \times \boldsymbol{B}) \times \boldsymbol{B}}{\mu_0 e n_e} \right] + \nabla \times \left(\frac{\nabla p_e}{e n_e} \right) \tag{3}$$

which, in addition to field convection (first term on the right-hand side), also includes resistive diffusion, the Hall effect, and the thermal source for magnetic fields. Various models for the plasma resistivity are available. They comprise classical anisotropic resistivity,[19] including contributions from electron–neutral collisions applicable to weakly ionized gases[17] and several anomalous resistivity models.

The set of MHD equations is completed by an equation-of-state function, which can be either analytic (e.g., ideal gas) or tabular. The latter is provided by the SESAME library, which includes semiempirical models for the thermodynamic properties, transport coefficients (including opacities), and average ionization state under local thermodynamic equilibrium.[20]

The level of sophistication and capability of the MACH2 code has been instrumental in providing invaluable insights into a variety of plasma problems. Some of these include plasma opening switches,[21] inertial-confinement fusion and alternative concepts,[22] compact toroid formation and acceleration schemes,[17] gas and solid density z-pinch implosion physics,[23] laser–target interactions,[24] high-power plasma source design,[25] magnetic nozzles,[26] and a variety of plasma thrusters.[11,19] Its diverse successes establish the code as a primary numerical tool for the understanding and development of efficient megawatt-class MPD thruster designs.

Megawatt-Class, Self-Field MPD Simulations

In an effort to provide code validation and useful insights, MACH2 was employed to model real MW-class thrusters in order to compare to experimental data. The particular thruster selected for the simulations was one of the Japanese MY[27,28] family of MPD configurations, which was operated with and without external magnetic fields. In this manner, MACH2 could be compared to both self-field and eventually applied-field operation within the power levels of interest.

Experimental Overview

The simulations examined the MY-II version[27] of the thruster, a schematic of which is shown in Fig. 1 (middle) along with the relative dimensions. The cathode was constructed of 2%-thoriated tungsten ($2.8\ \text{V} < \Phi_{\text{Th-W}} < 3\ \text{V}$) and the anode was mostly copper ($\Phi \sim 4.7$ V) interjected with 1-mm slits filled with ceramic material. It was operated with hydrogen propellant injected at a 50:50 ratio through two gas-feed ports adjacent to the electrodes [see Fig. 1 (middle)] at a mass-flow rate of 1.37 g/s. The power supply provided a 0.6-ms pulse at a maximum of 62 kJ, which allowed thruster operation at quasi-steady current levels of 4–18 kA, corresponding to

power levels of approximately 0.5–6 MW. The experimental data for self-field operation included thrust and discharge voltage, along with B-probe measurements that allowed mapping of the current distribution for the 10-kA case. In addition, erosion tests were performed, which showed insignificant anode-material loss and Th–W cathode losses on the order of 230 μg/shot (39.5 μg/C). Even though these values are still significant relative to mission-of-interest durations, other cathode materials[28] tested showed reduced erosion rates without affecting performance. Thermal characterization based on experimental measurements was also carried out by mapping electrode surface temperature. The 10-kA analysis computed cathode surface temperatures in the range of 1600–2600 K and anode temperatures of 600–1500 K. No evidence of onset was reported in the regime of operation. Thrust values varied in the range of $12\ \text{N} \le T \le 75\ \text{N}$ for $11.7\ \text{kA}^2\text{-s/g} \le J^2/\dot{m} \le 236.5\ \text{kA}^2\text{-s/g}$ and corresponding efficiencies of 0.08 at 4 kA to 0.36 at 18 kA.

A preliminary analysis based on the experimental findings is helpful in identifying significant characteristics of the thruster's behavior and provides some guidelines for the physical modeling. A comparison of the electromagnetic-force component based on the Maecker formula with $\delta = \frac{3}{4}$, $3.85\ \text{N} \le T_{\text{EM}} \le 78\ \text{N}$, implies a significant electrothermal-force component at lower discharge currents, which in turn suggests a transition from a predominantly electrothermal thruster to an electromagnetic accelerator as power is increased. Thus, it is critical that modeling appropriately calculate overall heating, in particular the thermodynamic properties, transport, and current distribution.

It has been conjectured with some experimental support[29] that plasma speeds are limited by the so-called Alfvén critical speed, $U_c \equiv \sqrt{(2Q_i/m_i)}$. In particular, once the plasma velocity reaches this critical value no further increase is available until the gas is fully singly ionized. This critical ionization velocity has been linked to the MPD thruster in various ways, ranging from the obvious performance limitation to electrode ablation[30] and onset.[8] For hydrogen $U_c = 51.3$ km/s ($Q_i = 13.6$ eV for H), which indicates that the MY-II thruster's exhaust speeds approached this limiting value only at the maximum discharge-current level ($8.75\ \text{km/s} \le U_{\text{ex}} = T/\dot{m} \le 54.7\ \text{km/s}$). Thus, the thruster's performance is not limited by rapid ionization-energy deposition (operation at exhaust speeds equal to the critical ionization speed is sometimes referred to as nominal) and full ionization is not anticipated. In addition, the power required to dissociate and fully ionize the hydrogen propellant ($Q_i = 15.4$ eV for H_2) at 1.37 g/s exceeds 2 MW, which supports the argument even at higher discharge currents.

Physical Modeling

The physics included in the MACH2 simulations modeled a viscous fluid with thermal nonequilibrium and real equation of state for hydrogen, supplied by the SESAME tables. The no-slip boundary condition was employed at the electrode surfaces, whereas thermal conduction was assumed at a constant temperature of 2000 K for the cathode and 1000 K for the anode, consistent with the aforementioned experimentally deduced data. Backplate mass injection employed a new parabolic-density scheme to approximate experimental mass feed in the vicinity of the electrodes. Mass was injected at sonic speeds for hydrogen at 300 K. The magnetic field boundary condition at the backplate prescribes the desired constant current for steady-state simulations; i.e., the toroidal field condition is that of a perfect insulator where the normal component of current disappears, $B_\theta(r, 0) = \mu_0 J/2\pi r$. The electrode surfaces are modeled as idealized conductors. The normal component of the magnetic field and the tangential component of the electric field must be continuous; i.e., the toroidal current density vanishes and magnetic induction is prescribed by $\boldsymbol{n} \cdot \nabla(r B_\theta) = 0$. The computational region was extended well downstream of the thruster's exit [see Fig. 1 (bottom)] in order to capture plume processes and impose uniform outlet boundary conditions (i.e., zero-gradient boundary conditions). Computations with a shorter extension of the computational region downstream of the thruster's exit [$L_g = 200$ mm as opposed to $L_g = 300$ mm; see Fig. 1 (bottom)] have shown negligible effects. However, the longer computational region was adopted

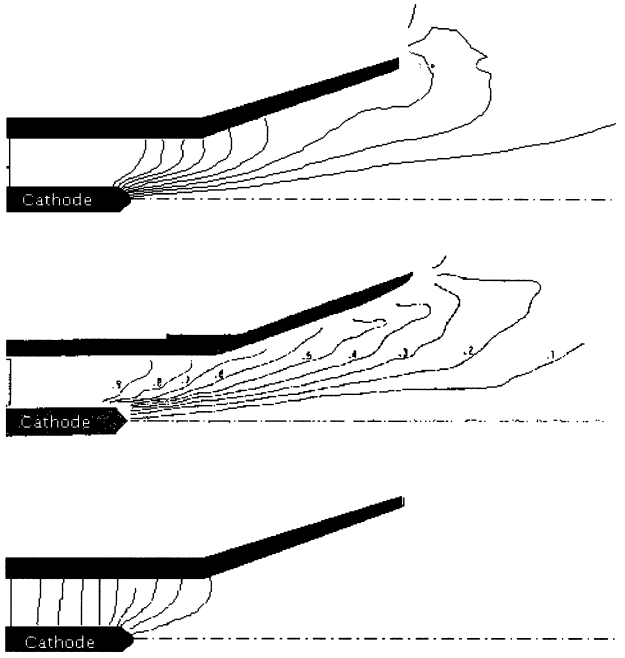

Fig. 2 Current distribution at 10 kA. Each contour represents a 10% increment. Top: MACH2 simulation with electron–neutral collisions included in the resistivity model. Thrust = 36.9 N, voltage = 183 V. Middle: Experiment; thrust = 34 N, voltage = 200 V, efficiency = 21%. Bottom: MACH2 simulation with classical resistivity. Thrust = 32.4 N, voltage = 108 V.

in all simulations in order to capture all available experimental current mappings (Fig. 2). Deposition of energy into different modes was calculated at the outlet boundaries in the following manner:

$$\text{Axial thrust: } T_z = \int \left(p + \frac{B^2}{2\mu_0} + \rho u_z^2 \right) \mathrm{d}A_z \tag{4}$$

$$\text{Radial force: } F_r = \int \left(p + \frac{B^2}{2\mu_0} + \rho u_r^2 \right) \mathrm{d}A_r \tag{5}$$

$$\text{Ionization power: } P_{\text{INZ}} = \left(\frac{Q_i}{m_H} \right) \int \rho \zeta \bar{u} \cdot \overline{\mathrm{d}A} \tag{6}$$

$$\text{Thermal power: } P_{\text{THE}} = \int \rho (e_H + e_e) \bar{u} \cdot \overline{\mathrm{d}A} \tag{7}$$

$$\text{Thermal conduction power: } P_{\text{TBC}} = \int (\kappa_i \bar{\nabla} T_i + \kappa_e \bar{\nabla} T_e) \cdot \overline{\mathrm{d}A}_{\text{elctrds}} \tag{8}$$

The thrust calculation properly includes contributions due to static and magnetic pressures; however, the computational region was sufficiently extended downstream of the thruster's exit so that these contributions were found to be negligible. Axial-thrust power P_z and radial-force power P_r were deduced from Eqs. (4) and (5), respectively, by utilizing $P = T^2/2\dot{m}$. The ionization energy per particle Q_i includes the energy to dissociate (i.e., $Q_i = 15.4$ eV), and thermal-conduction power represents the losses to the electrodes modeled to conduct heat at constant temperature.

Current was assumed to be constant, as the modeling focuses on steady-state operation, which was computationally reached within 0.5–1 ms. Steady state was confirmed by both the evolution of integrated variables and the evolution of two-dimensional distributions to a constant value. Computational stability (for the explicit schemes) and accuracy (for the implicit schemes), along with previous grid sensitivity analyses[11] for similar SF-MPD configurations and parameters, guided the choice for the computational grid's density. Specifically, the code adjusts the timestep based on a user's choice of Courant number, where for magnetic-field evolution the characteristic speed is the Alfven speed, $B/\sqrt{(\rho\mu_0)}$. For increased

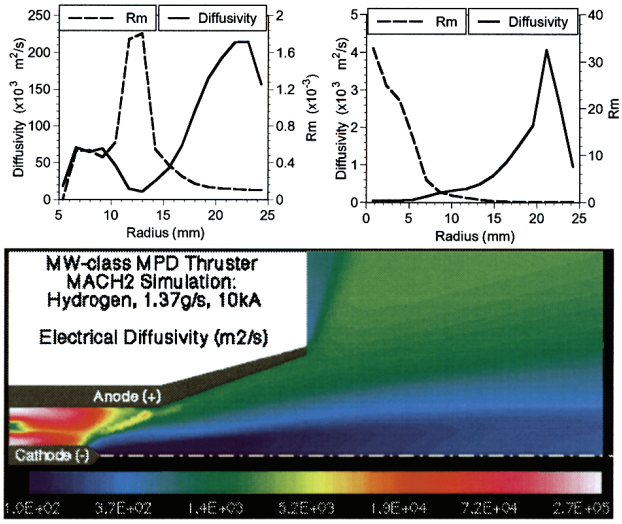

Fig. 3 Magnetic (electrical) diffusivity distribution and radial profiles for 10 kA. Axial locations: top left: 20 mm (midcathode); top right: 75 mm (end of anode straight section).

accuracy of the implicit schemes the Courant number was set to 0.9, which implies that the characteristic convection dimension δ_c scales with grid-cell dimension Δ as $\delta_c/\Delta = B/\sqrt{(\rho\mu_0)}]/(0.9U)$, where U is the flow's characteristic speed. For typical values of the 10-kA case, $B \sim 0.2T$, $\rho \sim 10^{-5}$ kg/m^3, $U \sim T/\dot{m} \sim 25$ km/s, and the ratio is 2.5, which means that 2.5 grid cells are utilized to resolve characteristic gradients due to field convection. On the other hand, for regions dominated by field diffusion (i.e., $\tilde{\eta} \sim 5 \times 10^3$ m^2/s from Fig. 3), the limited timestep resolves the associated characteristic gradients as follows: The characteristic diffusion dimension is $\delta_d = \sqrt{(\tilde{\eta}\Delta t)} \sim 5$ mm, for typical timesteps of the order of 5 ns. The grid-cell dimension was prescribed to be 1.875 mm which implies gradient resolution also on the order of 2.5 for field diffusion. Similar considerations ensure adequate gradient resolution for other physical processes.

Flow Characterization

Comparisons of the steady-state simulations to the experimental data for a discharge current of 10 kA (Fig. 2) were quite favorable for the case that utilized enhanced electrical transport and provided new insights that demanded further investigation. Principally, they have identified the importance of electron–neutral collisions in this high-density regime of operation, especially with respect to energy deposition. In particular, the MACH2 model of the plasma's magnetic diffusivity $\tilde{\eta} = (1/\mu_0\sigma)$ (also referred to as electrical diffusivity) includes contributions from such collisions as follows (shown in scalar form):

$$\tilde{\eta} = 1.0328 \times 10^{-4}\left(\bar{\zeta}\,\ell_n \Lambda \Big/ \mu_0 T_e^{\frac{3}{2}}\right) + (\sigma_e/\mu_0 e)[(1-\zeta)/\zeta]\sqrt{m_e T_e/q}\ (\mathrm{m^2/s}) \tag{9}$$

For hydrogen the electron–neutral collision cross section, σ_e was taken at 5×10^{-19} m^2 as a reasonable average over a range of electron energies.[31] The first term represents the electron–ion Coulomb encounters, i.e., the Spitzer formulation, while the second is additive and accounts for electron–atom collisions. This second term dominates transport inside the straight section of the discharge chamber, elevating magnetic diffusivity to values exceeding 2.0×10^5 m^2/s (Fig. 3). When compared to typical Spitzer values—the diffusivity is approximately $10^3/T_e^{3/2}$, where the electron temperature is in eV, so for 1 eV it is about 1000 m^2/s: it reaches as high as 200 times the expected Spitzer value. In turn, this implies that magnetic-field diffusion dominates the straight section and current conduction is forced downstream of the cathode tip. Indeed, the statement is confirmed by Fig. 3, which displays the radial profiles of the magnetic diffusivity and the magnetic Reynolds number (the characteristic length was taken at 20 mm) at two different axial locations: at midcathode and at the end of the anode's straight section. At the middle of the straight section between the two electrodes, R_m does not exceed $0.002 \ll 1$, which suggests fast magnetic-field diffusion and axially uniform azimuthal field. Alternatively, the ratio $U/\tilde{\eta}$ allows us to approximate the characteristic length at which we expect current conduction; i.e., for $R_m \sim 1$, $\ell_c = \tilde{\eta}/U \sim 10$ m, which basically suggests that magnetic-field convection becomes significant well downstream of the anode straight section. On the other hand, the approximation based only on Spitzer/coulombic transport would have implied $\ell_c \sim 5$ cm, suggesting current conduction inside the straight section, which is disproved by the experimental findings. Of course the behavior changes dramatically as the flow enters the cathode tip region and eventually the diverging section of the anode. In this region both the increase in volume and the electromagnetic pinching forces provide a lower density regime that diminishes the contributions from the electron–neutral collisions, thus enhancing electrical conductivity and allowing current flow. This is verified by the radial profiles of the diffusivity and R_m (Fig. 3) at the end of the anode's straight section. For the most part resistivity is due to electron–ion collisions with high magnetic Reynolds number, allowing convection of the magnetic field and explaining the current distention observed by the experimental (and theoretical) current mapping (Fig. 2). The current pattern observed is noteworthy with respect to the cathode attachment and implicit erosion rates. Additional comparisons of the current distribution over the cathode (Fig. 4) elaborates on the accuracy of the modeling and suggests the diminished contribution to energy losses through fall voltage. We note that attachment is limited to the cathode tip as opposed to the entire surface, implying reduced energy deposition and possibly electrode erosion rates. It should be noted that the logarithmic scale is responsible for an apparent discrepancy in the experimental and theoretical comparisons as we proceed toward the backplate. Even though, graphically, the discrepancy appears substantial it does not exceed 1% of the maximum value.

Further support is provided by interrogation of the MACH2 calculated average degree of ionization (Fig. 5), which shows that ionization was less than 10^{-4} in the straight section of the discharge chamber. Electron–ion collisions do not dominate and thus magnetic flux transport is governed by the second term of the magnetic diffusivity expression, which accounts for electron–neutral interaction. The two-dimensional distribution indicates that the propellant is significantly ionized far downstream of the backplate—which alleviates any concerns with the capability to numerically capture the short characteristic ionization scale-size evident in lower density thrusters—and only in the vicinity of the cathode tip and the lower density zone extending downstream of the tip. This is, of course, once again a consequence of the current pattern, which suggests that elevated heating can only occur downstream of the cathode tip, along with the associated ionization. At the thruster's exhaust only

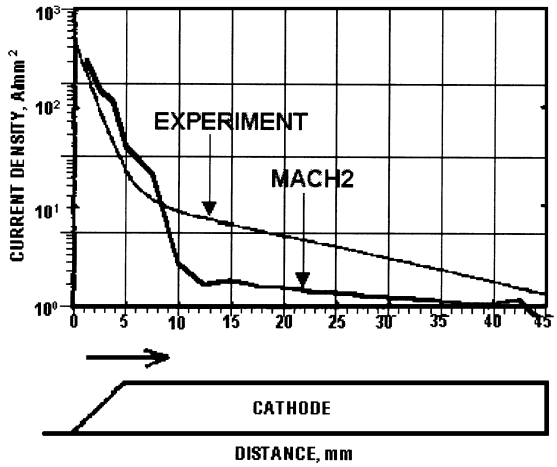

Fig. 4 Current density distribution over the cathode surface (J = 10 kA).

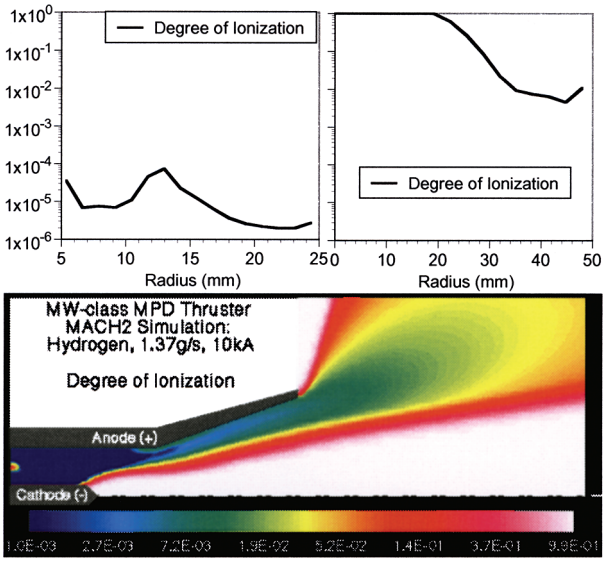

Fig. 5 Average degree of ionization distribution and radial profiles for 10 kA. Axial locations: top left: 20 mm (midcathode), top right: 104 mm (thruster exhaust).

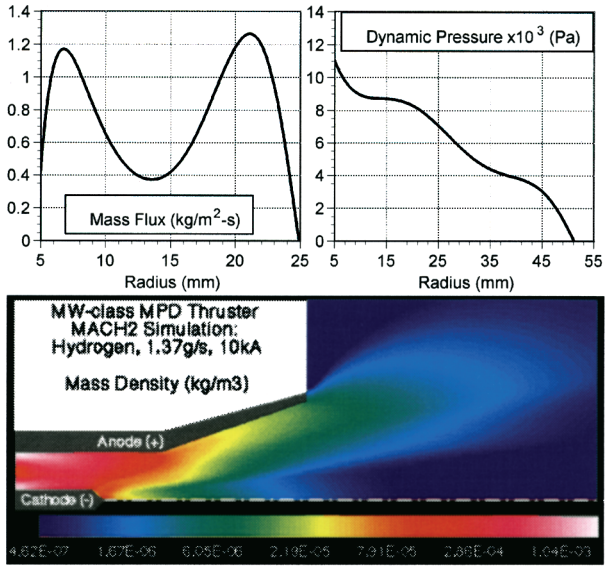

Fig. 6 Mass-density distribution and radial profiles for 10 kA. Axial locations: top left: 20 mm (midcathode); top right: 104 mm (thruster exhaust).

a portion of the hydrogen is fully ionized, constrained in the faster and lower-density region extending from the cathode tip. This is consistent with the aforementioned expectation that even at these higher power levels we should not expect full ionization, thus suggesting reduced energy deposition in the ionization internal modes. Examination of the mass density distribution (Fig. 6) in conjunction with the degree of ionization outlines the basic acceleration behavior. The two-dimensional distribution clearly demonstrates that the bulk of the propellant is exhausted in a region closer to the anode with a degree of ionization less than 0.1. The radial profile of the dynamic pressure, ρu^2, at the thruster's exhaust [Fig. 6 (top right)] supports the conclusion that the main thrust contribution is provided by this higher density, incompletely ionized hydrogen. We should also infer that this higher mass plasma in the vicinity of the anode diminishes the possibility of substantial power deposition through sheaths, as the electron-number densities are substantially reduced. The mass flux profile at midcathode [Fig. 6 (top left)] shows the elevated values previously inferred in the argument for inclusion of the electron–atom collisions along with the maintained influence of the propellant injection scheme. The latter does not substantially influence the thruster's behavior; however, this is due to this particular thruster's higher-density operation. The MACH2 upgrade to include mass-injection schemes will undoubtedly be significant in future approaches to lower-density MPD thrusters.

Power Budget, Thrust, and Voltage Comparisons

The characterization provided by the analysis and interrogation of the two-dimensional flow-field computed by MACH2 along with the comparisons of current mapping identified the significance of electron–neutral collisions and their consequent augmentation of electrical transport. These new insights also have significant ramifications involving power deposition and ultimately overall performance. Exclusion of electron-neutral collisions in calculating electrical resistivity suggests that the major energy losses are due to fall voltages and other external circuit losses, as the calculated plasma voltage dramatically underestimates the total experimental voltage. Specifically, the difference of 92 V between the calculated plasma voltage and the experimental total voltage suggests that such losses are on the order of 0.92 MW; in other words, almost half the available power is not deposited into the plasma and thus has no opportunity to be converted to useful thrust power.

On the other hand, inclusion of such physics substantially elevates the plasma voltage (and thus plasma power deposition), implying that the predominant inefficiencies are due to frozen-flow losses. This is accurately illustrated by a power budget that accounts for individual energy deposition to different modes and for external losses. This is given as follows, with the value in parentheses corresponding to values calculated under transport that does not account for electron–atom collisions:

Axial thrust power = 0.5 MW (0.377 MW)
Radial force power = 0.123 MW (0.08 MW)
Ionization power = 0.608 MW (0.352 MW)
Thermal power = 0.445 MW (0.251 MW)
Electrode conduction = 0.154 MW (0.027 MW)
External power = 0.17 MW (0.92 MW)

Comparison of the two scenarios shows that the Spitzer-modeled flow-field has electrode losses due to thermal conduction and other external losses (e.g., sheaths, circuit elements) on the order of 0.95 MW, as opposed to only 0.32 MW when the resistivity is enhanced. Comparison of the two-dimensional current distribution to the experiment shown in Fig. 2 supports adopting the formulation that includes electron–neutral-augmented transport. It is noteworthy that comparisons of the total thrust alone could not have offered such understanding or suggested inclusion of the improved model for the magnetic diffusivity, as the two calculated thrust values cannot be distinguished within experimental error.

The overall trends of the performance of this version of the MY-II thruster and further understanding of the acceleration and power-loss mechanisms can be deduced from comparisons of the calculated and experimental thrust and voltage data for a range of discharge currents. The calculated steady-state thrust-power ($P = T^2/2\dot{m}$) values are compared to the experimental ones in Fig. 7, along with the analytic approximation of the electromagnetic contribution to the thrust power based on Maecker's formula with $\delta = \frac{3}{4}$. They are very encouraging in both trends and magnitudes, especially at the higher current levels, adding to confidence in the current distribution comparisons. The discrepancy evident at lower power levels

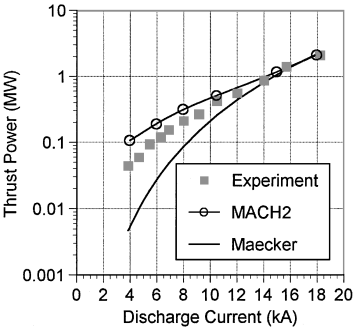

Fig. 7 Comparisons of the MACH2-calculated thrust power with experimental data for a range of discharge currents.

Table 1 Relevant Power Ratios

Current, kA	$(P_{INZ}+P_{THE}+P_{TBC})/P_{TOTAL}$	P_{EXT}/P_{TOTAL}	P_{EM}/P_Z
4	0.78	~0.0	0.042
10	0.59	0.083	0.424
18	0.395	0.18	1.075

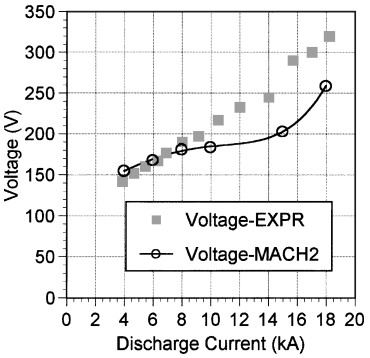

Fig. 8 Comparisons of MACH2-calculated plasma voltage to experimental total voltage.

will be addressed later. Comparisons with the Maecker magnitudes imply an increasingly significant electrothermal component as the power levels are decreased; the trend suggests that in this range of discharge currents the thruster switches from a predominantly electrothermal thruster to an electromagnetic accelerator.

The more revealing comparisons are those of experimental total voltage and MACH2-calculated plasma voltage; they are displayed in Fig. 8. The varying discrepancy with discharge current implies the relative significance of external energy losses and frozen-flow energy deposition. Specifically, at lower current levels the difference between plasma and total voltage is minimal, suggesting that the main losses are due to energy deposition to the internal modes as opposed to external losses. As the power level is increased the discrepancy increases, implying an increasing power deposition to the electrodes and a diminishing percentage to the internal energy modes: thermal, dissociation, and ionization. This in turn can be related to the relatively dominant thrust component as thruster operation transitions from mainly electrothermal to an electromagnetic accelerator. The argument can be further clarified by examining the ratio of electromagnetic thrust power to total thrust power, P_{EM}/P_Z (P_{EM} from the Maecker formula in Fig. 7), in relation to the voltage comparisons and other relative power deposition ratios as shown in Table 1.

It is noted that as P_{EM}/P_Z increases toward unity, external losses become more significant (total voltage-plasma voltage), while when the same ratio is close to zero such losses are minimal if not nonexistent. The latter can certainly occur if the plasma potential is equal to the electrode potential. It is more likely, though, that the numerical model overestimates the plasma power deposition at the lower power levels, which is consistent with the discrepancy noted in the thrust–power comparisons. This can be attributed to the use of an average collision cross section for the electron–neutral collisions in the resistivity expression as opposed to a more accurate and decreasing cross section as the energy is decreased. However, this does not detract from the general insights gained from this comparison. In particular, for the maximum discrepancy of 0.06 MW observed at 4 kA the calculated plasma voltage would be reduced by 15 V, which in turn would suggest that external power deposition is represented by a voltage of only 9 V compared to the total experimental voltage of 150 V.

The ratio of power deposited to frozen flow and lost through electrode thermal conduction decreases with increasing current and power level, while the projected external voltage losses increase. This occurs as the thruster transitions from mainly electrothermal at 4 kA ($P_{EM}/P_z = 0.042$) to approximately equally electrothermal and electromagnetic at 10 kA and mainly electromagnetic at 18 kA ($P_{EM}/P_z = 1.075$). The ratio P_{EM}/P_z is greater than one simply because the Maecker formula is an approximation with almost arbitrary choice of the additive term, taken in Eq. (1) as $\frac{3}{4}$. Thus, these comparisons suggest that the losses during electrothermal operation are mainly frozen-flow losses, which can be reduced by proper expansion of the flow, as in a solid converging–diverging nozzle. On the other hand, external voltage losses (e.g., electrode falls, circuit elements) increase with power level; however, for this thruster's operation regime and geometry they are not detrimental and any frozen-flow recoveries from proper nozzle design will benefit its performance. This is of course due to the fact that the thruster operates in a regime where plasma resistivity is dominated by an additive term due to atom–electron collisions, which in turn elevates the power deposited to the plasma and minimizes sheath losses. This provides the opportunity to recover some of the energy to useful thrust, as opposed to alternate operations during which the major percentage of the available power cannot be deposited to the plasma, but rather is expended to energy sinks such as fall voltage losses. It should be emphasized that expansion of the flow through a converging–diverging nozzle is not expected to provide major recovery of the energy expended to ionize; however, partial thermal-energy- and radial-momentum-loss recovery will be available. Such recoveries imply proper design of a converging–diverging nozzle that eliminates divergence losses, as opposed to the diverging nozzle used by the MY-II. Viscous losses for such a redesigned nozzle will not be detrimental, due to the high-mass-flux operation of this thruster; specifically, the viscous Reynolds number is on the order of 20,000, which implies a laminar boundary layer thickness of less than $\frac{3}{4}$ mm. Furthermore, geometry and operation manipulations with such a configuration will allow ample control of the current distribution and identification of optimal operation, during which ionization deposition is reduced, as opposed to recovered.

Conclusions

Numerical simulations of a megawatt-class, self-field MPD thruster were performed with the MACH2 code in order to validate the model and provide useful insights toward improving performance. Experimental data for thrust power, voltage, and current distribution were available for the necessary comparisons, which were very convincing regarding the validity of the physical model. Two-dimensional current distribution comparisons determined that modeling with Spitzer transport is inadequate; rather, atom–electron collisions dominate in such a manner as to substantially increase the plasma resistivity. This in turn predicted elevated plasma power deposition and minimal external losses, such as fixed circuit-element losses and electrode losses due to fall voltages. The dominant energy loss was calculated to be frozen-flow even though it decreased with increasing discharge current. Further confirmation can be realized by inclusion of a self-consistent fall voltage model; however, based on these insights, it is proposed that performance improvements can be achieved by expanding the flow through an appropriately designed converging–diverging nozzle.

References

[1]Maecker, H., "Plasma Jets in Arcs in a Process of Self-Induced Magnetic Compression," *Zeitschrift für Physik*, Vol. 141, No. 1, 1955, pp. 198–216.

[2]Jahn, R. G. "Magnetogasdynamic Description," *Physics of Electric Propulsion*, McGraw–Hill, New York, 1968, pp. 240–246.

[3]Tikhonov, V. B., Semenihin, S. A., Alexandrov, V. A., Dyakonov, G. A., and Popov, G. A., "Research of Plasma Acceleration Processes in Self-field and Applied Magnetic Field Thrusters," Paper IEPC-93-076, Electric Rocket Propulsion Society, Worthington, OH, Sept. 1993.

[4]Sovey, J. S., and Mantenieks, M. A., "Performance and Lifetime Assessment of MPD Arc Thruster Technology," NASA TM 101293 and AIAA Paper 88-3211, June 1988.

[5]Myers, R. M., Mantenieks, M. A., and LaPointe, M. R., "MPD Thruster Technology," NASA TM 105242 and AIAA Paper 91-3568, July 1991.

[6]Uematsu, K. J., Mori, K., Kunikaka, H., and Kuriki, K., "Effects of Electrode Configuration on MPD Arcjet Performance," 17th International Electric Propulsion Conf., Japan Society for Aeronautical and Space Sciences, Tokyo, 1984, pp. 79–86.

[7]Burton, R. L., Clark, K. E., and Jahn, R. G., "Measured Performance of a Multimegawatt MPD Thruster," *Journal of Spacecraft and Rockets*, Vol. 20, No. 3, 1983, pp. 299–304.

[8]Preble, J. C., "Onset in Magnetoplasmadynamic Thrusters: A Model of Electrothermal Instability," M.S. Thesis, Dept. of Aeronautics and Astronautics, Massachusetts Inst. of Technology, Cambridge, MA, May 1990.

[9]Ageyev, V. P., and Ostrovsky, V. G., "High-Current Stationary Plasma Accelerator of High Power," IEPC Paper 93-117, Electric Rocket Propulsion Society, Worthington, OH, Sept. 1993.

[10]Mikellides, P. G., Turchi, P. J., and Roderick N. F., "Applied-Field MPD Thrusters, Part 1: Numerical Simulations Using the MACH2 Code," *Journal of Propulsion and Power*, Vol. 16, No. 5, 2000, pp. 887–893.

[11]Mikellides, P. G., "A Theoretical Investigation of Magnetoplasmadynamic Thrusters," Ph.D. Dissertation, Dept. of Aeronautical and Astronautical Engineering, Ohio State Univ., Columbus, OH, Dec. 1994.

[12]Mikellides, P. G., and Turchi, P. J., "Applied-Field MPD Thrusters, Part 2: Analytic Expressions for Thrust and Voltage," *Journal of Propulsion and Power*, Vol. 16, No. 5, 2000, pp. 894–901.

[13]Peterkin, R. E., and Frese, M. H., *MACH: A Reference Manual—First Edition*, U.S. Air Force Research Lab., Kirtland AFB, NM, July 1998.

[14]Frese, M. H., MACH2: A Two-Dimensional Magnetohydrodynamics Simulation Code for Complex Experimental Configurations, AMRC-R-874, Mission Research Corporation, Albuquerque, NM, Sept. 1986.

[15]Peterkin, R. E., Jr., and Frese, M. H., "A Material Strength Capability for MACH2," MRC/ABQ-R-1191, Mission Research Corporation, Albuquerque, NM, Oct. 1989.

[16]Braginskii, S. I., "Transport Processes in a Plasma," *Review of Plasma Physics*, edited by M. A. Leontovich, Consultants Bureau, New York, 1965.

[17]Degnan, J. H., Peterkin, R. E., Jr., Baca, G. P., Beason, J. D., Bell, D. E., Dearborn, M. E., Dietz, D., Douglas, M. R., Englert, S. E., Englert, T. J., Hackett, K. E., Holmes, J. H., Hussey, T. W., Kiuttu, G. F., Lehr, F. M., Marklin, G. J., Mullins, B. W., Price, D. W., Roderick, N. F., Ruden, E. L., Sovinec, C. R., and Turchi, P. J., "Compact Toroid Formation, Compression, and Acceleration," *Physics of Fluids* B, Vol. 5, No. 8, 1993, pp. 2938–2958.

[18]Douglas, M. R., "Radiation Production from Stagnating Compact Toroids Employing a Nonequilibrium Radiation Diffusion Model," Ph.D. Dissertation, Dept. of Nuclear Engineering, Univ. of New Mexico, Albuquerque, May 1994.

[19]Turchi, P. J., Mikellides, I. G., Mikellides, P. G., and Kamhawi, H., "Pulsed Plasma Thrusters for Microsatellite Propulsion: Techniques for Optimization," *Micro-Propulsion for Small Spacecraft*, Progress in Astronautics and Aeronautics, American Inst. of Aeronautics and Astronautics, Reston, VA, Vol. 19, 2000, Chap. 14, pp. 353–368.

[20]Holian, K. S. (ed.), "T-4 Handbook of Material Properties Data Base. Vol Ic: EOS," Los Alamos National Lab., LA-1160-MS, Los Alamos, NM, Nov. 1984.

[21]Buff, J., Peterkin, R. E., Jr., Roderick, N. F., Degnan, J. H., Frese, M. H., and Turchi, P. J., "Enhancement of the Radiation Yield in Plasma Flow Switch Experiments," Mission Research Corp., MRC/ABQ-R-1171, Albuquerque, NM, 1988; also *IEEE Transactions on Plasma Science*, Vol. 19, No. 3, 1991, pp. 502–509.

[22]Peterkin, R. E., Jr., "Simulations of Staged Solid Shell Implosions to Produce Fusion," AIAA Paper 95-2899, July 1995.

[23]Degnan, J. H., Lehr, F. M., Beason, J. D., Baca, G. P., Bell, D. E., Chesley, A. L., Coffey, S. K., Dietz, D., Dunlap, D. B., Englert, S. E., Englert, T. J., Gale, D. G., Graham, J. D., Havranek, J. J., Holmberg, C. D., Hussey, T. W., Lewis, R. A., Outten, C. A., Peterkin, R. E., Jr., Price, D. W., Roderick, N. F., Ruden, E. L., Shumlak, U., Smith, G. A., and Turchi, P. J., "Electromagnetic Implosion of Spherical Liner," *Physical Review Letters*, Vol. 74, No. 1, 1995, pp. 98–101.

[24]Stamper, J. A., Ripin, B. H., Peterkin, R. E., Jr., and Stellingwerf, R. F., "Aneurisms in Laser-Driven Blast Waves," *Physics of Fluids*, Vol. 31, No. 11, 1988, pp. 3353–3361.

[25]Mikellides, P. G., Turchi, P. J., and Mikellides, I. G., "Design of a Fusion Propulsion System, Part 1: Gigawatt-Level Magnetoplasmadynamic Source," *Journal of Propulsion and Power*, Vol. 18, No. 1, 2002, pp. 146–151; also IEPC Paper 99-013.

[26]Mikellides, I. G., Mikellides, P. G., Turchi, P. J., and York, T. M., "Design of a Fusion Propulsion System, Part 2: Numerical Simulation of Magnetic-Nozzle Flows," *Journal of Propulsion and Power*, Vol. 18, No. 1, 2002, pp. 152–158; also AIAA Paper 2000-3367, 2000.

[27]Tahara, H., Kagaya, Y., and Yoshikawa, T., "Quasi-Steady MPD Arcjets with Applied Magnetic Fields," AIAA Paper 85-2001, July 1985.

[28]Tahara, H., Kagaya, Y., and Yoshikawa, T., "Quasi-Steady Magnetoplasmadynamic Thrusters with Applied Magnetic Fields for Near-Earth Missions," *Journal of Propulsion*, Vol. 5, No. 6, 1989, pp. 713–719.

[29]Alfvén, H., "Collision Between a Nonionized Gas and Magnetized Plasma," *Reviews of Modern Physics*, Vol. 32, No. 4, 1960, pp. 710–713.

[30]Turchi, P. J., "Critical Speed and Voltage–Current Characteristics in Self-Field Plasma Thrusters," *Journal of Propulsion and Power*, Vol. 2, No. 5, 1988, pp. 398–401.

[31]Brode, R. B., "Energy Dependence of Electron–Atom Elastic Cross Sections," *Reviews in Modern Physics*, Vol. 5, 1933, pp. 257–262.